AGU ADVANCING EARTH AND SPACE SCIENCE

Geophysical Research Letters

RESEARCH LETTER
10.1029/2021GL092510

Key Points:

- An integrative analysis is applied for the seismological and geodetic data of the 2020 Stanley, Idaho earthquake
- We found that the Stanley earthquake ruptured a pair of opposing-dip faults offset by a 10-km-wide step that narrows with depth
- This study reveals that complicated rupture processes appear to be typical for the earthquakes located near the northern Centennial Tectonic Belt boundary

Supporting Information:

Supporting Information may be found in the online version of this article.

Correspondence to:

J. Yang and H. Zhu,
jidong.yang@upc.edu.cn;
Hejun.Zhu@utdallas.edu

Citation:

Yang, J., Zhu, H., Lay, T., Niu, Y., Ye, L., Lu, Z., et al. (2021). Multifault opposing-dip strike-slip and normal-fault rupture during the 2020 M_w 6.5 Stanley, Idaho earthquake. *Geophysical Research Letters*, *48*, e2021GL092510. https://doi.org/10.1029/2021GL092510

Received 12 JAN 2021
Accepted 20 APR 2021

Multifault Opposing-Dip Strike-Slip and Normal-Fault Rupture During the 2020 M_w 6.5 Stanley, Idaho Earthquake

Jidong Yang[1], Hejun Zhu[2], Thorne Lay[3], Yufeng Niu[4], Lingling Ye[5], Zhong Lu[6], Bingxu Luo[2], Hiroo Kanamori[7], Jianping Huang[1], and Zhenchun Li[1]

[1]Department of Geophysics, China University of Petroleum (East China), Qingdao, China, [2]Department of Geosciences, University of Texas at Dallas, Richardson, TX, USA, [3]Department of Earth and Planetary Sciences, University of California, Santa Cruz, CA, USA, [4]School of Mining and Geomatics Engineering, Hebei University of Engineering, Handan, China, [5]Department of Earth and Space Sciences, Southern University of Science and Technology, Shenzhen, China, [6]Roy M. Huffington Department of Earth Sciences, Southern Methodist University, Dallas, TX, USA, [7]Seismological Laboratory, California Institute of Technology, Pasadena, CA, USA

Abstract On March 31, 2020, an M_w 6.5 earthquake struck near Stanley, Idaho. More than 35% nondouble-couple component in long-period point-source solutions indicate a more complex source than slip on a planar fault. Using an integrative analysis of seismological and geodetic data, we find that the Stanley earthquake ruptured a pair of opposing-dip faults offset by a 10-km-wide step, including an unmapped northern subfault with predominantly strike-slip faulting and a southern subfault subparallel to the Sawtooth fault with predominantly normal faulting. This converging fault geometry allowed the rupture to traverse a surficial 10-km-wide step, which is greater than the limiting dimension (3–4 km) that commonly ceases earthquake ruptures. This study reveals that a composite rupture process with strike-slip and normal faulting is typical for earthquakes located near the northern boundary of the Centennial Tectonic Belt (CTB), which is distinct from the predominantly normal faulting in the central CTB.

Plain Language Summary The northwest of Stanley, Idaho, is struck by an Mw6.5 earthquake on March 31, 2020, which is the largest event in Idaho since the 1983 Borah Peak earthquake. This event has several intriguing aspects: (1) the epicenter located by USGS is not on a mapped fault and the source region has little historical seismicity over the past 50 years; (2) it predominantly involves strike-slip faulting, which is inconsistent with the extensional strain accommodated by the closest Sawtooth fault; (3) long-period point-source solutions have more than 35% non-double-couple components, indicating a more complex source than slips on a planar fault. Based upon an integrative analysis for both seismological and remote sensing data, we prescribe an opposing-dip two-fault model to reconcile all observations. The rupture initiated near the USGS epicenter, and then propagated to the southeast about 20 km along the northerner subfault trajectory. When reaching the northwestern terminus of the Sawtooth fault, the rupture changed its original trajectory and moved southwestward, traversing a 10-km-wide step-over. After passing the mapped Sawtooth fault terminus, it propagated to the southeast about 25 km along the southern subfault, which is subparallel to the Sawtooth fault scarp.

1. Introduction

At 23:52:31 (UTC) on March 31, 2020, the Salmon-Challis National Forest was struck by an M_w 6.5 earthquake, ~30 km NNW of Stanley, Idaho. This was the largest event (Figure 1) in the state since the 1983 M_w 6.9 Borah Peak earthquake (Doser & Smith, 1985). The mainshock occurred in the southern part of the Northern Rocky Mountains province, which is characterized by several active normal faults that have produced Pleistocene to Holocene ruptures (Barton et al., 2003; Thackray et al., 2013). The closest major fault recognized in this area is the Sawtooth fault (Haller et al., 2004), a northwest-trending and east-dipping normal fault, which separates the Stanley basin to the northeast from the uplifted Sawtooth Mountains to the southwest. The epicenter of the Stanley earthquake estimated by the U.S. Geological Survey (USGS) National Earthquake Information Center (NEIC) is 115.118°W, 44.465°N, about 16 km from the northwestern terminus of the mapped Sawtooth Fault. In addition, the mainshock involves predominantly strike-slip

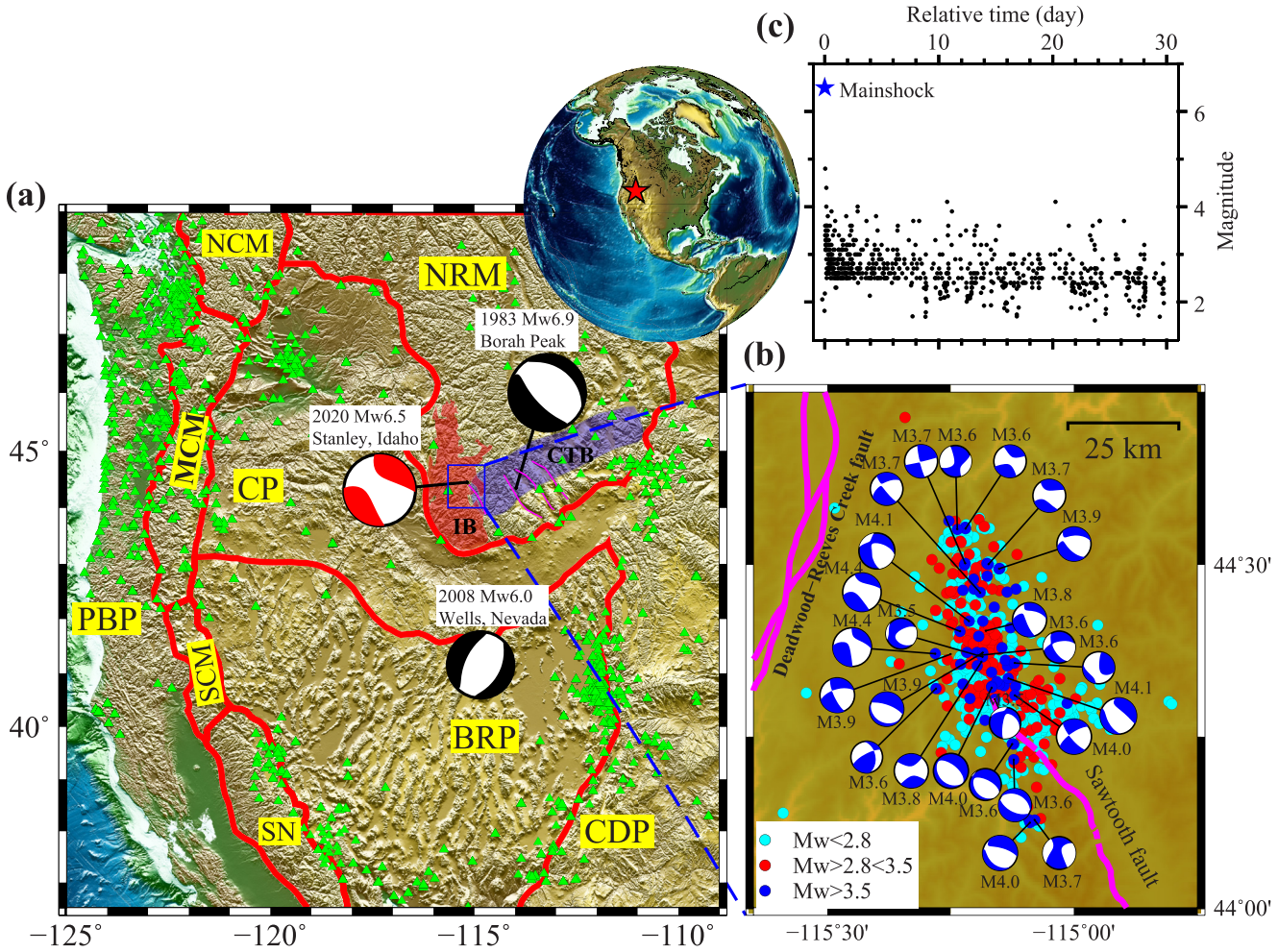

Figure 1. Topographic map with tectonic provinces around the 2020 M_w 6.5 Stanley earthquake. (a) Geological provinces and historic large earthquakes in the vicinity of the 2020 Stanley earthquake. Green triangles denote seismological stations used in back-projection. Red shading region denotes the Idaho Batholith (IB). Blue shading area shows the Centennial Tectonic Belt (CTB). Magenta solid lines are the Sawtooth, Lost River, Lemhi and Beaverhead faults (from left to right). (b) Aftershocks within 1 month after the mainshock from the USGS-NEIC catalog, and focal mechanisms for events with magnitude greater than 3.5 (https://earthquake.usgs.gov/earthquakes/search/). The northern aftershocks are dominated by strike-slip faulting, and the southern aftershocks near the Sawtooth fault involve normal faulting. (c) Magnitude-time evolution of the aftershocks. Blue star denotes the mainshock. Abbreviations for tectonic structures are: NRM, Northern Rocky Mountains. CP, Columbia Plateau. BRP, Basin and Range Province. PBP, Pacific Border Province. CDP, Colorado Plateaus. NCM, MCM, and SCM, Northern, Middle and Southern Cascade Mountains. SN, Sierra Nevada.

faulting, inconsistent with rupture of an extension of the Sawtooth normal fault. These observations suggest that the 2020 earthquake involved at least one previously unmapped Quaternary fault.

Early ground surveys were inhibited by heavy snowfall, and summertime investigations failed to detect any surface rupture of the M_w 6.5 Stanley earthquake (Liberty et al., 2020). Thus, we rely on seismological and geodetic observations to quantify the faulting. Long-period point-source moment tensor solutions have predominantly strike-slip focal mechanisms with significant nondouble-couple components (Table 1). The Global centroid moment tensor (GCMT) and the USGS-NEIC *W*-phase solution have similar best-double-couple solutions with strike (ϕ), dip (δ) and rake (λ) given for both possible planes in Table 1. The centroid depth (d) estimates range from 13.8 to 19.5 km, and the centroid time shift (t_c) from 4.5 to 7.2 s. We perform an independent *W*-phase inversion (Kanamori & Rivera, 2008) using 108 global recordings filtered in the frequency band 0.005–0.01 Hz, and find a moment tensor similar to the USGS-NEIC solution, but with slightly lower seismic moment (M_0) and centroid depth (Table 1). All three moment tensors have large deviations from a single double-couple of 35%–44%. When constraining the solution to be a pure double-couple,

Table 1
Long-Period Point-Source Moment Tensor Parameters

	$M_0(10^{18}$ Nm)	M_w	ϕ_1 (°)	δ_1 (°)	λ_1 (°)	ϕ_2 (°)	δ_2 (°)	λ_2 (°)	d (km)	t_c (s)	NDC (%)
GCMT	6.39	6.47	174.0	72.0	−19.0	270.0	72.0	−161.0	13.8	7.2	43
NEIC W-phase	6.67	6.48	172.2	74.0	−23.8	269.1	67.2	−162.7	19.5	4.5	44
Our W-phase	6.0	6.45	172.3	70.7	−24.3	270.8	67.1	−158.9	9.5	8.0	35

Note. M_0 is the Scalar moment, M_w is the moment magnitude, ϕ_i, δ_i, and λ_i ($i = 1, 2$) denote the strike, dip, and rake of two nodal planes. d denotes depth, t_c is the centroid time, NDC is the nondouble-couple component. Global Centroid moment Tensor (GCMT) solution is downloaded from https://www.globalcmt.org/CMTsearch.html, USGS-NEIC W-phase solution is download from https://earthquake.usgs.gov/earthquakes/eventpage/us70008jr5/executive.

we find the *W*-phase waveform fitting to be considerably degraded, suggesting that the nondouble-couple components are stable features in these point-source solutions.

One typical explanation for the nondouble-couple component is geometrically complex shear faulting (Frohlich, 1994; Julian et al., 1998) with multiple differently oriented fault planes. An increasing number of multifault ruptures during a single event have been documented with improved geodetic and seismological observations over the past decade (Ammon et al., 2005; Black & Jackson, 2008; Eberhart-Phillips et al., 2003; Ross, Idini, et al., 2019; Wesnousky, 2006). Documented multifaulting (Hamling et al., 2017; Wei et al., 2011; Zhang et al., 2012) can occur in interlocked active fault networks during large earthquakes (typically most observable for events with magnitude greater than 7.0). The March 31, 2020, Stanley earthquake has an intermediate magnitude (M_w ~6.5), and the epicenter is not on a mapped fault, instead it locates in a region with little historical seismicity over the past 50 years. We seek to determine the fault geometry and rupture process that can account for significant (>35%) nondouble-couple component in long-period inversions for this event. Here, we present an integrated analysis of the fault geometry, rupture process, slip history and subfault focal mechanisms, using state-of-the-art methods in seismology (moment tensor decomposition, high-resolution 3D back-projection, deep-learning-assisted double-difference aftershock relocation, and multifault slip teleseismic inversion) and remote sensing (multifault inversion of interferometric synthetic aperture radar, InSAR). We consider the tectonic setting of the compound faulting that we determine and the implications for regional seismic risk.

2. Methods

2.1. High-Resolution Regional Multiazimuth Back-Projection

Good-coverage and high-quality seismic data (green triangles in Figures 1 and S1a) recorded by the Federation of Digital Seismic Network (FDSN) and Global Seismic Networks (GSN) provide an opportunity to image the coseismic rupture process of the 2020 M_w 6.5 Stanley earthquake using high-resolution multiazimuth back-projection (Yang et al., 2020). In data preprocessing, we applied manual data-quality checking, noisy trace removal, instrument response deconvolution, bandpass filtering in the frequency band of 0.2–5 Hz, surface wave cutting and amplitude normalization. Then, we use the fast marching method (Sethian & Popovici, 1999) to calculate the traveltime from each station to potential subsurface sources in a 3D crustal and uppermost mantle velocity model (Shen & Ritzwoller, 2016). Finally, an imaging method similar to Kirchhoff migration (Kiser & Ishii, 2017; Yang et al., 2020) is applied to vertical-component *P* wave records to constrain the space-time distribution of energy release. A 3D region of 100 × 100 × 40 km, including the hypocenter, is discretized into 200 × 200 × 200 cells with horizontal and vertical spacings of 0.5 and 0.2 km. We assume that all nodes of the grid are potential sources, and compute the back-projection results using the following imaging condition (Nakata & Beroza, 2016; Sun et al., 2016) as

$$I(\mathbf{x},\tau) = \prod_{i_{az}=1}^{N_{az}} \int_{\tau-\Delta t}^{\tau+\Delta t} \sum_{\mathbf{x}_r(i_{az})} U_z\left(\mathbf{x}_r(i_{az}), t' + t(\mathbf{x}_r,\mathbf{x})\right) dt' \quad (1)$$

where $I(\mathbf{x},\tau)$ is the imaging volume at the rupture time of τ, $U_z(\mathbf{x}_r,t)$ denotes the processed vertical-component seismogram, and $t(\mathbf{x}_r,\mathbf{x})$ is the traveltime from station $\mathbf{x}_r$ to potential source location $\mathbf{x}$. $\mathbf{x}_r(i_{az})$ denotes the station belonging to the ith azimuthal cluster, and N_{az} is the total number of azimuthal clusters. The

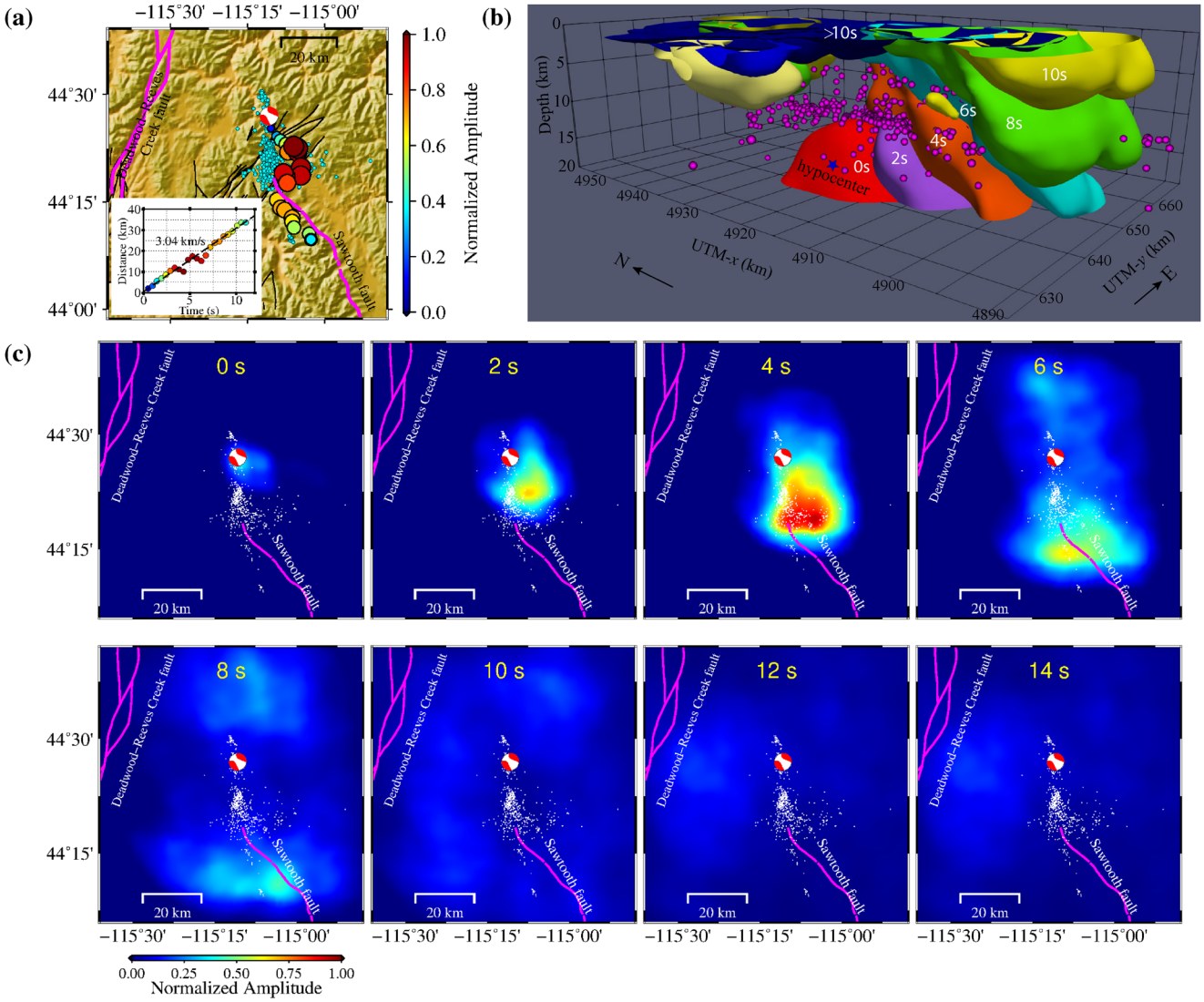

Figure 2. Coseismic rupture during the M_w 6.5 Stanley earthquake imaged by regional multiazimuth back-projection. (a) Rupture trajectory calculated using the peak radiated energy locations. The inset shows the epicentral distance versus propagation time. Cyan dots are the relocated aftershocks using the double-difference location method, and black curves denote the Trans-Challis fault system. Panels (b) and (c) show the rupture processes imaged by the back-projection at different times in 3D (isosurfaces) and map views, respectively. The purple dots in (b) and white dots in (c) are relocated aftershocks. Radiated energy amplitudes are normalized such that the maximum value is unity.

multiplication of the imaging results from different azimuths is used to suppress imaging artifacts and improve spatial resolution (Figures 2 and S1).

2.2. Finite-Fault Inversion for Teleseismic Data

We invert broadband teleseismic body waves for several kinematic models using a linear least squares kinematic inversion (Hartzell & Heaton, 1983; Kanamori & Rivera, 2008; Ye et al., 2016). The teleseismic data include 72 *P* wave and 37 SH-wave ground displacement recordings that are filtered in the frequency band from 0.005 to 0.9 Hz (Figure S3). The structural model used in the inversion is the local model (Bremner et al., 2019; Christian Stanciu et al., 2016; Davenport et al., 2017; Laske et al., 2013). We use spatial smoothing, and down weight SH signals by a factor of five relative to P signals to balance the overall signal power. The subfault source time functions are parameterized with 12 1-s rise-time symmetric triangles offseted by 1-s intervals, allowing up to 13 s rupture durations for each 3-km by 4.5-km subfault. The allowed

maximum rupture velocity is set to 4 km/s. The subfault durations and rupture velocity are both relatively large for the small subfault dimensions, but this is allowed in order to accommodate the uncertainty in the hypocentral position.

Using *P* wave traveltimes of 17 regional stations, we relocate the mainshock and obtain an estimate of 44.376°N, 115.221°W and 13 km deep, with uncertainties of 3.2 km along latitude, 6.9 km along longitude and 4.1 km in depth. The relocated result deviates from the USGS-NEIC mainshock hypocenter about 8.4 km to the southwest. For the relocated epicenter at 44.376°N and 115.221°W, the source depth has to be adjusted to 18.75 km to lie on the constrained kinematic model (Figures 3 and S4). Inversion with this depth of a hypocenter places slip too deep on the fault and too far to the north to account for InSAR surface deformation, along with producing degraded fits to teleseismic waveforms. Moving the hypocenter up-dip to a depth of 13 km at 44.383°N, 115.20°W improves the fit to close to that for a single fault model, but still places the main slip north of the area with largest surface deformation. A final hypocentral adjustment to 44.33°N, 115.18°W and 13 km deep in the finite-fault inversion is made to bring the InSAR and teleseismic models into good agreement. The regional *P* wave motions indicate a low-amplitude onset of motions, which may be below detection in teleseismic data affecting the USGS-NEIC hypocenter estimate and alignment of such data for finite-fault inversion, so we rely on the superior location sensitivity of the InSAR observations to guide this adjustment.

2.3. InSAR Analysis for the European Space Agency Sentinel-1 Data

We use a two-pass differential InSAR approach (Massonnet et al., 1993; Rosen et al., 2000) to process ascending and descending data acquired by the European Space Agency (ESA) Sentinel-1 satellite. The ascending image pair was acquired on March 20 and April 7, 2020, with perpendicular baseline of 63 m and temporal baseline of 18 days. The descending images were acquired on November 7, 2019 and May 5, 2020, with perpendicular baseline of 109 m and temporal baseline of 180 days. To improve the coherence of image pairs and to avoid potential phase jumps between bursts of Sentinel-1, we have applied precision image co-registration to ensure registration accuracy higher than 0.001 of one pixel in the azimuth. We use a SRTM (Shuttle Radar Topography Mission) 1 arc sec (~30 m) digital elevation model (Farr et al., 2007) to simulate and remove the topographic phase. Then, the interferograms are multilocked by a factor of 16 in range and 4 in azimuth (~54 m × 56 m), filtered to suppress decorrelation noises (Goldstein & Werner, 1998) and unwrapped using the minimum cost-flow method (Chen & Zebker, 2000). To reduce atmospheric turbulence phase and the effect of orbit errors, we have applied the GACOS (Generic Atmospheric Correction Online Service) production and the quadratic polynomial regression, successively. Finally, the displacement fields are geocoded onto the WGS-84 geographic coordinate.

2.4. Deep-Learning-Assisted Double-Difference Aftershock Relocation

Furthermore, we collected 1-month (from March 31 to April 30, 2020) continuous seismic data from 44 real-time seismometers near the mainshock epicenter, during which 662 aftershocks were detected by the USGS-NEIC (https://earthquake.usgs.gov/earthquakes/search/). The moment magnitudes of these aftershocks range from 1.61 to 4.8. Data processing before traveltime picking include demeaning, detrending, resampling, bandpass filtering in the frequency band from 1 to 20 Hz and amplitude normalization. Since the origin time of aftershocks in the USGS-NEIC catalog might be inaccurate, we first use the short-term-average and long-term-average ratio to determine the event time (Withers et al., 1998), and then cut corresponding waveforms within a time window of 4 s from the continuous dataset. Windowed waveforms are then used as inputs for a trained Convolutional Neural Network to automatically pick the first *P* wave arrivals (Ross, Meier, & Hauksson, 2018). Once all *P* wave traveltimes of 44 stations are extracted, a double-difference earthquake location approach (Waldhauser & Ellsworth, 2000) is used to relocate these aftershocks. Because the double-difference relocation utilizes the inner connection of different events located in similar tectonic environment, 49 aftershocks are considered as outliers due to weak linkages with other events. The distributions of the remaining 613 relocated aftershocks are more clustered than those from the USGS-NEIC catalog, which helps to further delineate the fault geometry (Figure S7).

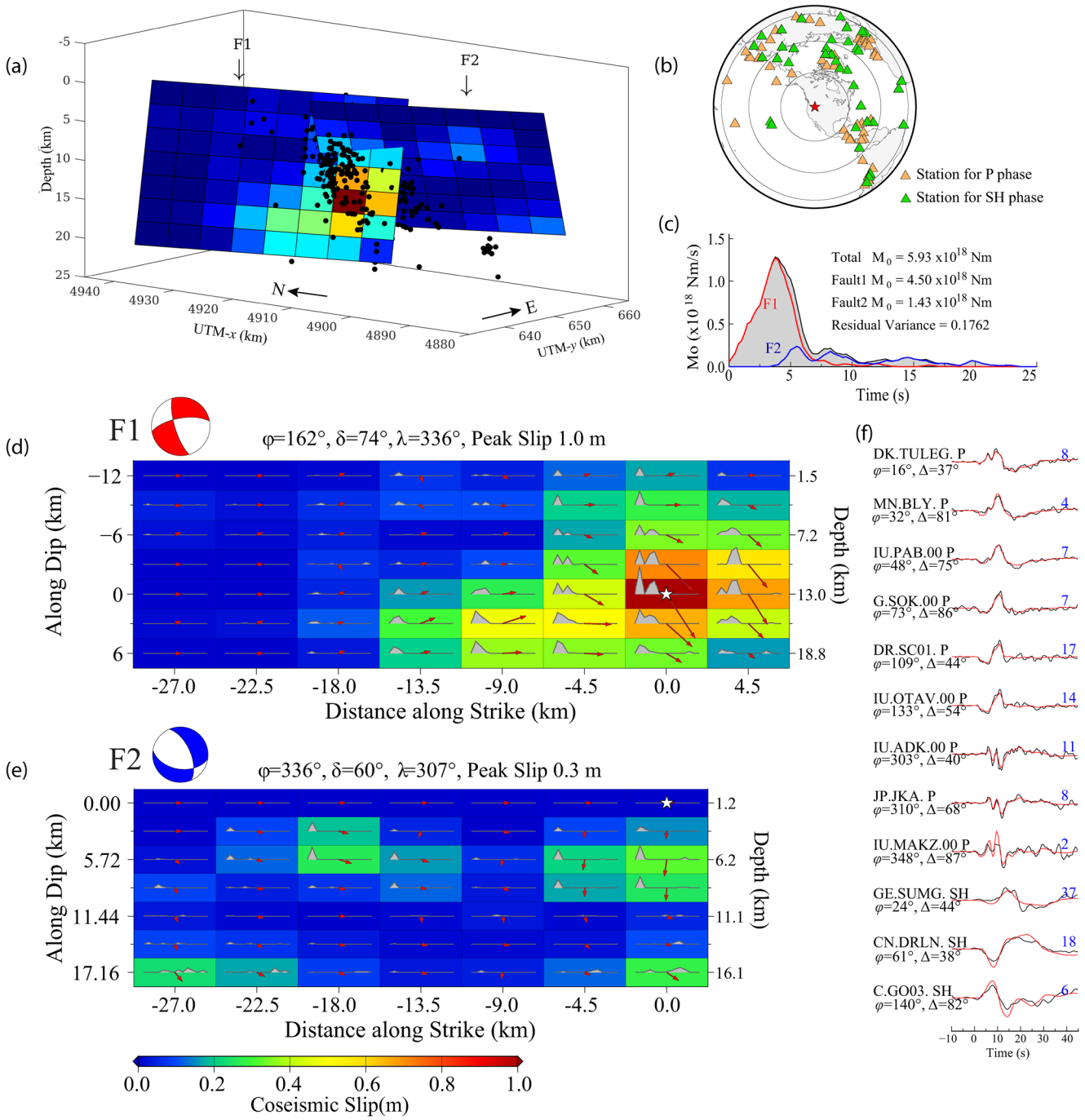

Figure 3. Two-fault kinematic slip solution from teleseismic finite-fault inversion. (a) 3D visualization of the fault geometry and slip distributions. Black dots are relocated aftershocks. (b) Station locations for teleseismic P (orange) and SH (green) phases used in the finite-fault inversion. (c) Moment rate function for individual faults (red for F1, blue for F2) and the composite faulting process (gray). (d, e) Detailed slip distributions for the two faults, showing the rake (vector orientations on the fault plane), slip magnitudes (vector length and color scale) and subfault source time functions (gray polygons with a maximum time extent of 13 s). (f) Representative P and SH waveform fitting results (black for observed, red for predicted) in the frequency band of 0.005–0.9 Hz. Station name, phase type, azimuth and epicentral distance are shown to the left. Peak amplitude in microns is shown in blue on the right. More waveform comparisons can be found in Figure S5.

3. Analysis and Results

For the *W*-phase solution from the USGS-NEIC, we apply various moment tensor decompositions (Vavryčuk, 2015). For a double-couple plus compensated linear vector dipole (CLVD) decomposition, strike-slip faulting dominates with 44% CLVD (Table S1). The intermediate eigenvalue is negative with a plunge of 62–64° at an azimuth of 311–320°, which indicates an additional normal-faulting contribution. Decomposition into major and minor double-couples indeed finds a normal-faulting minor component. Decomposition into three double-couples yields predominantly strike-slip, moderate oblique normal, and minor thrust mechanisms (Table S1). These nonunique decompositions show that the significant nondouble-couple component is associated with combined strike-slip and normal faulting.

Next, we use the regional back-projection results to constrain the fault geometry and coseismic rupture processes. The multiazimuth back-projection results reveal a "Z-shape" rupture trajectory at the hypocenter depth (Figures 2 and S1), including a pair of nearly parallel NW-SE trending segments offset at the surface by a 10-km-wide step. An average rupture speed of 3.0 km/s is estimated using a least squares regression between the epicentral distance and propagation time, which is about 83% of the local shear wave velocity (~3.6 km/s). The imaged rupture positions have good agreement with the distribution of relocated aftershocks (Figure 2) and asymmetry of surface strains calculated from the ESA Sentinel-1 data. High-frequency coherent radiation calculated with multiazimuth back-projection provides a detailed rupture process during the Stanley earthquake (Figure 2 and Movie S1). The event initiated southwest of the epicenter estimated by the USGS-NEIC, and then propagated to the southeast about 20 km. When reaching the vicinity of the northwestern terminus of the mapped Sawtooth fault after about 4 s, the rupture stopped propagating to the southeast, changed its original trajectory and moved southwestward. After the rupture passed the northern endpoint of the Sawtooth fault outcrop, it propagated to the southeast about 25 km along a trajectory subparallel to the Sawtooth fault scarp. The maximum high-frequency radiation occurred in the step-over area (Figures 2 and S1).

Guided by the fault geometries from point-source solutions, moment tensor decompositions, back-projection results, and InSAR displacement fields, we invert broadband teleseismic body waves for several finite-fault models (Figures 3 and S2–S5). An initial inversion with a single planar fault favors a nearly north-south trending nodal plane, as also found by the USGS-NEIC (https://earthquake.usgs.gov/earthquakes/eventpage/us70008jr5/finite-fault). The single-fault inversion (Table S2 and Figure S2) for the 172.3° striking fault plane from our *W*-phase inversion achieves a good fit to teleseismic P and SH waveforms (Figure S3). A subfault with peak slip of less than 1 m is concentrated near the hypocenter (set as the USGS-NEIC location), and the rake has minor variations in the region near the asperity (Figure S2b). The main pulse in the moment rate function has a duration of ~8 s. The spectrum of the moment rate function is combined with the stacked spectra of teleseismic broadband *P* waves (after corrections for radiation patterns and propagation effects) to compute a broadband source spectrum (Figure S2c). The radiated seismic energy is found to be about 1.72×10^{14} J, which is slightly larger than that computed by the IRIS (~1.1×10^{14} J, http://ds.iris.edu/spud/eqenergy/18107918). The static stress drop estimate for this model is 1.2 MPa (Figure S2e) using the estimation methods of Ye et al. (2016).

Although the single-fault model achieves good teleseismic data fits (residual variance = 0.169), it cannot explain the large nondouble-couple component in the long-period point-source solutions (Figure S2d). We found this to be the case for other single-fault inversions; all of them lack enough variability in rake to generate much nondouble-couple component of the composite source. The ability to match the data well with a single-plane model indicates that using teleseismic data alone cannot robustly resolve detailed source complexity responsible for the nondouble-couple component. In addition, the fault plane using the USGS-NEIC hypocenter shows a significant spatial shift from aftershock locations and surface displacement from InSAR. Therefore, we draw upon independent constraints from the back-projection results, lineations of relocated aftershocks and coseismic surface deformation to prescribe a two-fault model (Table S2) that can account for the full set of data while matching the full moment tensor (Figures 3–5). The two subfaults, F1 in the north and F2 in the south, have opposite dip and intersect in the step-over region (Figures 3 and S4, Movie S2). The peak slip of about 1 m is observed near the step-over at a depth of 13 km. There are minor variations in the rake around an average of 336°. The seismic moment on F1 is 4.5×10^{18} Nm. The rupture initiation location for the southern F2 is 1.23 km deep in the shallowest subfault to the northwest, with a

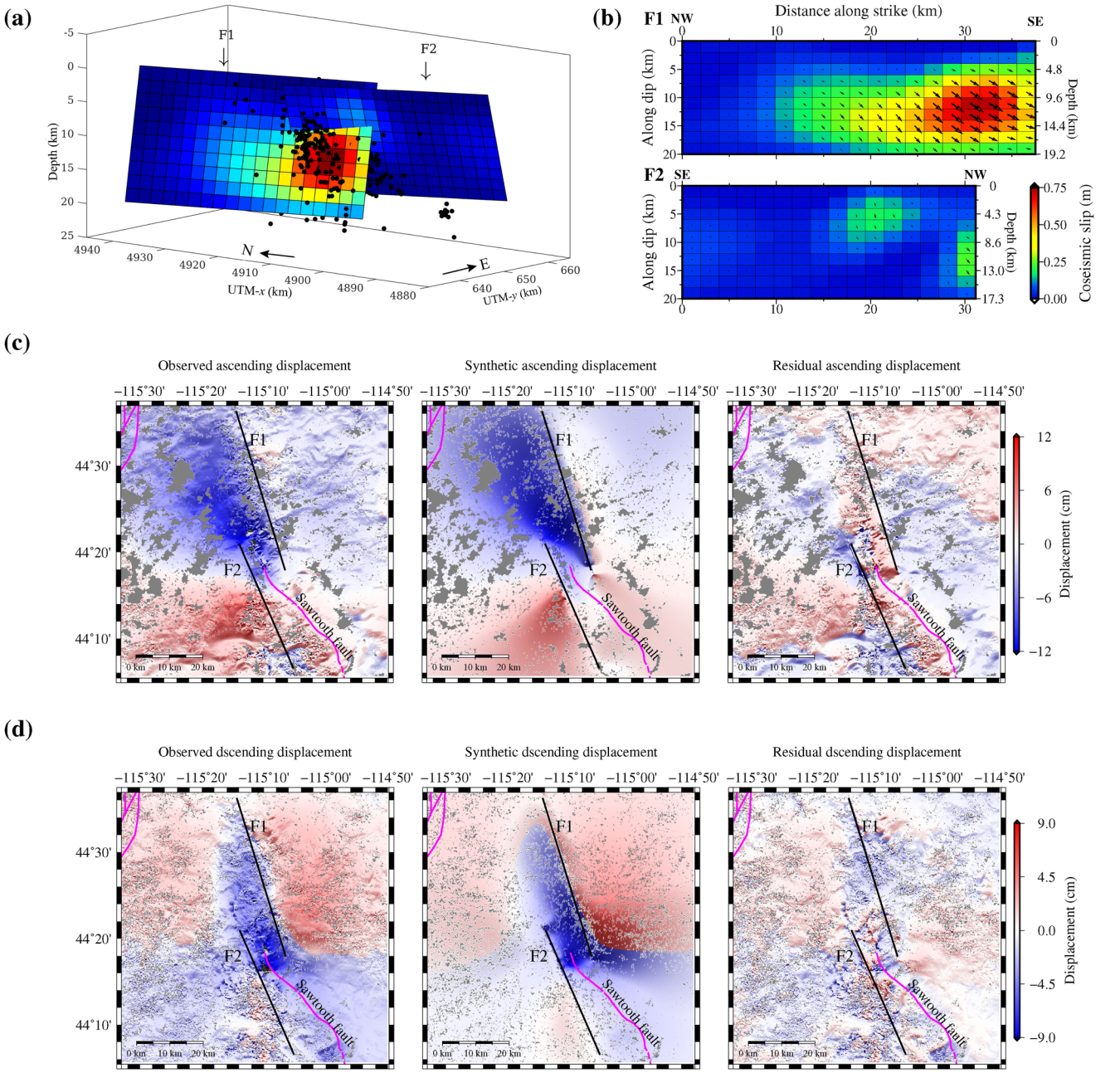

Figure 4. InSAR analysis results of the ESA Sentinel-1 data for the 2020 Stanley earthquake. (a) 3D visualization of the slip model, estimated using InSAR surface deformation inversion. Black dots denote relocated aftershocks. (b) Detailed slip distributions and rake directions on 2D fault planes. (c) Observed, synthetic and residual unwrapped displacements (from left to right) for the Sentinel-1 ascending track along the line-of-sight direction. Interferograms are computed using the image pair on March 20 and April 7, 2020. (d) Corresponding displacements for the Sentinel-1 descending track, and the image pair was acquired on November 7, 2019 and May 5, 2020.

2.9 s delay relative to the onset of faulting on F1. The average rake is 307°, corresponding to oblique normal faulting. The seismic moment on F2 is 1.43×10^{18} Nm, about one third of that for F1. The composite faulting has a seismic moment of 5.93×10^{18} Nm ($M_w = 6.45$). The overall moment rate function has a well-resolved interval of 7 s duration and minor poorly resolved features extending to 20 s (Figure 3c), in good agreement with the time function of stacked radiated energy in the back-projection (Figure S1b). The specific timing of the rupture on the two-faults is not well resolved, but is much shorter than 7 s. Predicted and observed seismograms for this two-fault model show good waveform matches (residual variance = 0.176, Figures 3f

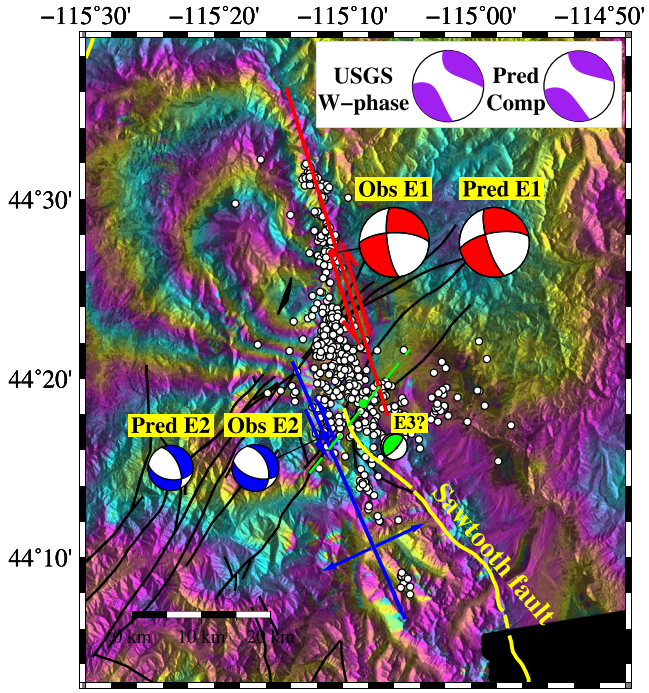

Figure 5. A conceptual fault model for the M_w6.5 Stanley earthquake. The background is the coseismic interferogram calculated from the ascending Sentinel-1 images. Red line denotes the left-lateral strike-slip F1, and the associated event (E1) generates a scalar moment of 4.5×10^{18} Nm. Blue line denotes F2 with predominantly normal faulting and slight strike-slip motions. The corresponding event (E2) produces a scalar moment of 1.43×10^{18} Nm. Compression in the intersection region might produce a small event (E3) with thrust faulting (F3 denoted by the dashed green line). Observed (Obs) moment tensors for F1 and F2 are calculated using the three-subevent moment tensor decomposition of the USGS-NEIC *W*-phase solution (Table S1). Predicted (Pred) moment tensors are computed from the slip model shown in Figure 3. Comparison of the predicted composite (Pred Comp) focal mechanism with the USGS *W*-phase solution is shown in the top right corner. White dots are relocated aftershocks within one month after the mainshock. Yellow lines denote the Quaternary faults, black lines are Trans-Challis faults.

and S3), comparable to those from the single-fault model. But the composite moment tensor (Figure 5 and S4) for the combined faulting on F1 and F2 is consistent with the long-period point-source solution. The geometry of the two faults is similar to that inferred from the lineations of seismicity (Liberty et al., 2020).

To further verify the viability of the opposing-dip two-fault model, we perform an independent geodetic inversion (Wang et al., 2013) using coseismic deformation fields, which are calculated using the InSAR analysis based on the synthetic aperture radar (SAR) data from the ESA Sentinel-1. Strike and dip angles of F1 and F2 in the InSAR analysis are set to be the same as those used in the seismic finite-fault inversion. The deformation fields from ascending and descending geometries are incorporated in a geodetic inversion to constrain the slip distributions on the two faults. Because near-field deformation can provide better spatial resolution than teleseismic data, we discretize the fault planes with finer subfaults than those in the seismic inversions. F1 has 19 1.97-km-long subfaults along strike and ten 2-km-wide subfaults along dip. The peak slip of ~0.74 m is found in the intersection with F2 at 11.5 km deep (Figure 4a and Movie S3). Estimated rakes on subfaults with slip greater than 0.2 m have minor deviations (±16°) from an average angle of 331°. The seismic moment of F1 is 4.7×10^{18} Nm, corresponding to an average stress drop ~1.01 MPa. F2 has 16 1.94-km-long subfaults along strike and ten 2-km-wide subfaults along dip. The maximum slip of 0.23 m is located to the northwest, and the average rake is about 309° with small variations. The seismic moment of F2 is 1.0×10^{18} Nm and the average stress drop is ~0.28 MPa. The two-fault model produces a composite seismic moment about 5.7×10^{18} Nm ($M_w = 6.44$) and achieves 96.5% data fitting for near-field displacements. Estimated rake and slip distributions both show good agreement with the seismic finite-fault solution, demonstrating the internal consistency of different datasets for the 2020 Stanley earthquake.

4. Discussion

Regional multiazimuth back-projection, which does not depend on any a priori knowledge of the fault geometry, reveals a "Z-shape" coseismic rupture trajectory. To reconcile observations of aftershock distribution, teleseismic records and near-field InSAR deformation, we prescribe a two-fault rupture model (Figure 5), which includes a northern 36-km-long fault (F1) with a strike of 162° and a dip of 74° (toward the southwest), and a southern 31.5-km-long fault (F2) with a strike 336° of and a dip of 60° (toward the northeast). The opposing dip of F1 and F2 causes them to intersect at depth close to the northern terminus of the mapped Sawtooth fault (Figure S4). Strike-slip displacement on F1 and oblique normal faulting on F2 produce a composite moment tensor solution with a large nondouble-couple component, in good agreement with the USGS-NEIC *W*-phase solution (Figure 5). In our model, the F2 subfault aligns along the lineations of vigorous seismicity within the footwall of the Sawtooth fault. It is not the Sawtooth fault, but a subparallel fault. Why there are multiple faults dipping eastward with different dips is still unclear and needs further investigations.

The irregularity in the correlation between epicentral distance and propagation time (Figure 2a) indicates that the rupture process was not a continuous propagation across these two faults. It appears that the rupture slowed down in the step-over region from 2.5 to 5 s, where is located in the Trans-Challis fault zone. The concentration of aftershocks in this area (Figure 5) also suggests the presence of complex faulting, with residual strains being released by the afterslip. One possible explanation for the stagnation of the rupture is that old breaks in the Trans-Challis fault zone were reactivated by the shear stress change on F1 during the

early ~3 s. The reactivation made it easier to release concentrated stresses along preexisting faults, which prevented the rupture on F1 from propagating further to the southeast. Instead, it dynamically triggered a new rupture on F2 subparallel to the Sawtooth fault outcrop (Thackray et al., 2013). The interaction of stress transfer from a northern unmapped fault across the Trans-Challis fault zone to a subparallel strand of the Sawtooth fault produced the "Z-shape" rupture trajectory.

Fault steps of 3–4 km are commonly considered as a limiting dimension that can cease earthquake rupture (Wesnousky, 2006). The 2020 Stanley earthquake appears to traverse a surficial 10-km-wide step and trigger a secondary rupture. But the step-over is likely much smaller at depth because of the converging fault geometries. From observations of the lineations of the relocated aftershocks in the step-over region, we have also considered a three-fault model, which includes an additional northeast-trending fault F3 that connects F1 and F2 (Figure 5). The geometry is prompted by the back-projection trajectory (Figure 2a) and the three double-couple decomposition of the moment tensor (Table S1). The F3 segment (Figure 5) aligns along the southern branches of the Trans-Challis fault system (Bennett, 1986; Liberty et al., 2020). Numerical experiments illustrate that the addition of F3 with geometry from the moment tensor decomposition produces a slightly degraded teleseismic waveform fitting (with residual variance = 0.204) in finite-fault modeling and less than 0.5% improvement in the geodetic inversion (Figure S6). Aftershocks in the step-over include some with a geometry of compressional faulting on a northeast-trending plane (Figure 1) similar to what we used as a trial geometry for F3, but there is a diversity of faulting geometries for aftershocks in the step-over. Lack of specific constraints on the faulting geometry in the step-over region leads us to prefer the two-fault coseismic rupture model, acknowledging uncertainty in the nature of deformation in the step-over. The cross fault F3 might accommodate some afterslip as shown by Pollitz, Hammond, and Wicks (2020). While F1 and F2 appear to intersect at depth (Figures 3 and 4), which may have helped the rupture negotiate the step-over, there is uncertainty in the specific triggering process.

Pollitz, Hammond, and Wicks (2020) proposed a kinematic model for this event according to the aftershock pattern, which is made up of a south-southeast striking segment and one/two cross fault segments. The south-southeast trending segment is similar to F1 in our model, which is dominated by left-lateral strike-slips. In addition, Pollitz, Hammond, and Wicks (2020) inferred that at least one northeast-trending fault accommodates a few decimeters of right-lateral afterslip. Although their model produces good fitting for regional strong motion waveforms, the predicted InSAR displacements do not correlate well with the observed displacement pattern. In contrast, we incorporate another segment F2 in our model, which is subparallel to the Sawtooth fault and accommodates normal-faulting slip. The composite geometry is consistent with the back-projection trajectory and lineations of related aftershocks, and it can produce good data fitting for both teleseismic waveforms and near-field InSAR displacements.

The long-period moment tensor solutions of the 2020 Stanley earthquake have greater than 35% nondouble-couple contribution. Commonly invoked mechanisms for large nondouble-couple components include unsteady fluid flow, dike intrusions, tensile faulting, fault complexity, heterogeneity, and anisotropy of the focal region (Julian et al., 1998). Since no active magma chambers have been observed in the source region, the unsteady fluid flow and dike intrusion processes can be excluded for the Stanley earthquake. Although there are some hot springs near Stanley (Druschel & Rosenberg, 2001), the moment tensor of the 2020 Stanley earthquake has such a large overall nondouble couple that minor geothermal activity cannot account for it. In addition, strong anisotropy sufficient to affect the long-period waves used in the moment tensor inversions is unlikely in the shallow crust of the Stanley earthquake region (Bremner et al., 2019; Christian Stanciu et al., 2016). Based on the back-projection results, InSAR ground deformation and aftershock distribution, we favor a multifault rupture process to explain the significant nondouble-couple in the moment tensors of the Stanley earthquake. This hypothesis is supported by the slip models from seismic and geodetic finite-fault inversions, for which the composite faulting results on F1 and F2 yield a moment tensor similar to the long-period point-source solutions.

Continuous Global Positioning System (GPS) measures an extensional ENE-oriented strain rate of $7.3 \pm 0.4 \times 10^{-9}$ yr^{-1} across the Centennial Tectonic Belt (CTB) of the Northern Basin and Range province (McCaffrey et al., 2013; Payne et al., 2012), which is mainly accommodated by four major normal faults (the Sawtooth, Lost River, Lemhi and Beaverhead faults). Fault morphology and gravity studies show that recent slip of the Sawtooth fault has concentrated along its northern trace, and the fault long-term activity

has shifted northward (Mabey et al., 1983; Pollitz, Hammond, & Wicks, 2020; Thackray et al., 2013). Therefore, similar to the 1983 M_w6.9 Borah Peak earthquake, the extensional strain in the CTB is one of the most important factors for the 2020 M_w6.5 Stanley earthquake. In addition, surface deformation studies based on GPS measurements (Payne et al., 2012) reveal that the southern Idaho Batholith (IB) moves to the west with a different velocity from the ENE-directed extension in the adjacent CTB. The different deformation orientations and rates may contribute to the strike-slip faulting during the Stanley earthquake, for which the epicenter is located at the boundary between the IB and the CTB blocks (Figure 1). The global CMT solutions of a historical 1983 M_w5.6 event with centroid location of 114.54°W and 44.75°N and a more recent 2014 M_w4.4 event with centroid location of 114.64°W and 44.79°N also involve predominantly strike-slip motion with normal-faulting components. In addition, Koper et al. (2018) and Pollitz, Wicks, et al. (2019) have reported that the shearing and extension also appeared along the mapped opposite-dip faults during the 2017 Sulfur Peak earthquake. Therefore, a composite rupture process involving strike-slip and normal faulting appears to be typical for earthquakes located near the northern CTB boundary, and even more typical for earthquakes along the northern Basin and Range fault zone. This observation suggests a systematic difference from the extension accommodated by predominantly normal faulting in the central CTB, both shearing and extensional strains are accumulated at the northern CTB boundary and are accommodated by combined strike-slip and normal faulting on unmapped faults or the northern segments of mapped normal faults.

The aftershock evolution from April to October (Figure S8) shows that overall seismicity activity gradually decreases with time after the mainshock. The aftershocks clustered near the northwestern terminus of the Sawtooth fault might be associated with the reactivation of the Trans-Challis faults (Pollitz, Hammond, & Wicks, 2020), and the collapse of the Stanley Lake Inlet Beach affected by the mainshock as reported by the Idaho Geological Survey. The seismicity near the southeastern end of F2 increased, especially in July and August, indicating that residually extensional strain was released by aftershocks. The Stanley earthquake illustrates that potentially damaging earthquake can occur away from the mapped active faults in central Idaho (Liberty et al., 2020). Future observations are important to monitor seismic activity in this region. A large earthquake on the Sawtooth fault, such as a M_w7.2 scenario earthquake simulated by the USGS-NEIC (https://earthquake.usgs.gov/scenarios/eventpage/bssc2014640_m7p16_se/executive), would produce both local and regional effects, including strong shaking in the town of Stanley (2020 population of 71), moderate shaking in the Boise metropolitan area (population of 749,202) and partial damage of heavily touristed moraine-dammed lakes (Thackray et al., 2013).

5. Conclusions

In this study, we present an integrative analysis for the 2020 Stanley earthquake using state-of-the-art methods in seismology and remote sensing. An opposing-dip two-fault model is prescribed to reconcile the observations of aftershock distribution, teleseismic records and near-field InSAR deformation, which includes an unmapped northern subfault with predominantly strike-slip faulting and a southern subfault subparallel to the Sawtooth fault with predominantly normal faulting. The converging fault geometry allows the rupture to traverse a surficial 10-km-wide step, which is greater than the limiting dimension (3–4 km) that commonly ceases earthquake ruptures. Considering tectonic settings, we infer that the composite ruptures involving both strike-slip and normal faulting appears to be typical for earthquakes located near the northern boundary of the CTB, which is different from the predominantly normal faulting in the central CTB. In addition, the vigorous seismicity indicates that the residual strains are continuously released after the Stanley mainshock, and damaging earthquakes might occur away from the mapped active faults.

Data Availability Statement

All data needed to evaluate the conclusions in this study are presented in the paper and supplement materials. Seismological data used in back-projection and finite-fault inversion can be downloaded from https://ds.iris.edu/wilber3/find_event. The 3D crustal velocity model used in back-projection analysis can be downloaded from http://ds.iris.edu/ds/products/emc-us2016/. The aftershock catalog is downloaded from https://earthquake.usgs.gov/earthquakes/search/. Sentinel-1 images used in InSAR analysis are provided

by the European Space Agency and can be downloaded from https://search.asf.alaska.edu/#/. We thank two anonymous reviewers and the editor G. Prieto for helpful comments on the manuscript.

Acknowledgments
This study is supported by the startup funding of Guanghua Scholar at China University of Petroleum (East China) (20CX06069A) (To Jidong Yang) and UTD faculty startup funding (to. Hejun Zhu). Thorne Lay's research on earthquake is supported by U.S. National Science of Foundation grant EAR1802364. Lingling Ye's research on earthquake is supported by National Natural Science Foundation of China (No. 41874056). Yufeng Niu's research on earthquake is supported by National Natural Science Foundation of China (No. 41901286). Jianping Huang and Zhenchun Li are supported by National Outstanding Youth Science Foundation (No. 41922028), National Natural Science Foundation of China (No. 41874149), and Funds for Creative Research Groups of China (No. 41821002).

References

Ammon, C. J., Ji, C., Thio, H.-K., Robinson, D., Ni, S., & Hjorleifsdottir, V., et al. (2005). Rupture process of the 2004 Sumatra-Andaman earthquake. *Science*, *308*(5725), 1133–1139. https://doi.org/10.1126/science.1112260

Barton, K. E., Howell, D. G., & Vigil, J. F. (2003). *The North America tapestry of time and terrain* (No. 2781). US Geological Survey.

Bennett, E. H. (1986). Relationship of the trans-Challis fault system in central Idaho to Eocene and Basin and Range extensions. *Geology*, *14*(6), 481–484. https://doi.org/10.1130/0091-7613(1986)14<481:ROTTFS>2.0.CO;2

Black, N. M., & Jackson, D. D. (2008). Probability of multifault rupture. *Bulletin of the Seismological Society of America*, *98*(6), 3017–3024. https://doi.org/10.1785/0120070271

Bremner, P. M., Panning, M. P., Russo, R. M., Mocanu, V., Stanciu, A. C., Torpey, M., et al. (2019). Crustal shear wave velocity structure of central idaho and eastern oregon from ambient seismic noise: Results from the IDOR project. *Journal of Geophysical Research: Solid Earth*, *124*, 1601–1625. https://doi.org/10.1029/2018JB016350

Chen, C. W., & Zebker, H. A. (2000). Network approaches to two-dimensional phase unwrapping: Intractability and two new algorithms. *Journal of the Optical Society of America*, *17*(3), 401–414. https://doi.org/10.1364/josaa.17.000401

Christian Stanciu, A., Russo, R. M., Mocanu, V. I., Bremner, P. M., Hongsresawat, S., Torpey, M. E., et al. (2016). Crustal structure beneath the Blue Mountains terranes and cratonic North America, eastern Oregon, and Idaho, from teleseismic receiver functions. *Journal of Geophysical Research: Solid Earth*, *121*, 5049–5067. https://doi.org/10.1002/2016JB012989

Davenport, K. K., Hole, J. A., Tikoff, B., Russo, R. M., & Harder, S. H. (2017). A strong contrast in crustal architecture from accreted terranes to craton, constrained by controlled-source seismic data in Idaho and eastern Oregon. *Lithosphere*, *9*(2), 325–340. https://doi.org/10.1130/l553.1

Doser, D. I., & Smith, R. B. (1985). Source parameters of the 28 October 1983 Borah Peak, Idaho, earthquake from body wave analysis. *Bulletin of the Seismological Society of America*, *75*(4), 1041–1051.

Druschel, G. K., & Rosenberg, P. E. (2001). Non-magmatic fracture-controlled hydrothermal systems in the Idaho batholith: South fork Payette geothermal system. *Chemical Geology*, *173*(4), 271–291. https://doi.org/10.1016/s0009-2541(00)00280-1

Eberhart-Phillips, D., Haeussler, P. J., Freymueller, J. T., Frankel, A. D., Rubin, C. M., Craw, P., et al. (2003). The 2002 Denali fault earthquake, Alaska: A large magnitude, slip-partitioned event. *Science*, *300*(5622), 1113–1118. https://doi.org/10.1126/science.1082703

Farr, T. G., Rosen, P. A., Caro, E., Crippen, R., Duren, R., Hensley, S., & Alsdorf, D. (2007). The shuttle radar topography mission. *Reviews of Geophysics*, *45*, RG2004. https://doi.org/10.1029/2005RG000183

Frohlich, C. (1994). Earthquakes with non-double-couple mechanisms. *Science*, *264*(5160), 804–809. https://doi.org/10.1126/science.264.5160.804

Goldstein, R. M., & Werner, C. L. (1998). Radar interferogram filtering for geophysical applications. *Geophysical Research Letters*, *25*(21), 4035–4038. https://doi.org/10.1029/1998GL900033

Haller, K. M., Machette, M. N., Dart, R. L., & Rhea, B. S. (2004). U.S. Quaternary fault and fold database released. *Eos, Transactions American Geophysical Union*, *85*(22), 218. https://doi.org/10.1029/2004EO220004

Hamling, I. J., Hreinsdóttir, S., Clark, K., Elliott, J., Liang, C., & Fielding, E., et al. (2017). Complex multifault rupture during the 2016 Mw 7.8 Kaikōura earthquake, New Zealand. *Science*, *356*(6334). https://doi.org/10.1126/science.aam7194

Hartzell, S. H., & Heaton, T. H. (1983). Inversion of strong ground motion and teleseismic waveform data for the fault rupture history of the 1979 Imperial Valley, California, earthquake. *Bulletin of the Seismological Society of America*, *73*(6A), 1553–1583.

Julian, B. R., Miller, A. D., & Foulger, G. R. (1998). Non-double-couple earthquakes: 1. Theory. *Reviews of Geophysics*, *36*(4), 525–549. https://doi.org/10.1029/98RG00716

Kanamori, H., & Rivera, L. (2008). Source inversion of W phase: Speeding up seismic tsunami warning. *Geophysical Journal International*, *175*(1), 222–238. https://doi.org/10.1111/j.1365-246x.2008.03887.x

Kiser, E., & Ishii, M. (2017). Back-projection imaging of earthquakes. *Annual Review of Earth and Planetary Sciences*, *45*, 271–299. https://doi.org/10.1146/annurev-earth-063016-015801

Koper, K. D., Pankow, K. L., Pechmann, J. C., Hale, J. M., Burlacu, R., Yeck, W. L., et al. (2018). Afterslip enhanced aftershock activity during the 2017 earthquake sequence near Sulfur Peak, Idaho. *Geophysical Research Letters*, *45*, 5352–5361. https://doi.org/10.1029/2018DL078196

Laske, G., Masters, G., Ma, Z., & Pasyanos, M. (2013). Update on CRUST1.0—A 1-degree global model of Earth's crust. *Geophysical Research Abstracts*, *15*, 2658.

Liberty, L. M., Lifton, Z. M., & Dylan Mikesell, T. (2020). The 31 March 2020 Mw 6.5 Stanley, Idaho, Earthquake: Seismotectonics and Preliminary Aftershock Analysis. *Seismological Research Letters*, *92*(2A), 663–678.

Mabey, D., Webring, M. W., & McIntyre, E. (1983). Regional geophysical studies in the Challis quadrangle. *Symposium on the geology and mineral deposits of the Challis*, *1*(2), 69–79.

Massonnet, D., Rossi, M., Carmona, C., Adragna, F., Peltzer, G., Feigl, K., & Rabaute, T. (1993). The displacement field of the Landers earthquake mapped by radar interferometry. *Nature*, *364*(6433), 138–142. https://doi.org/10.1038/364138a0

McCaffrey, R., King, R. W., Payne, S. J., & Lancaster, M. (2013). Active tectonics of northwestern U.S. inferred from GPS-derived surface velocities. *Journal of Geophysical Research: Solid Earth*, *118*, 709–723. https://doi.org/10.1029/2012JB009473

Nakata, N., & Beroza, G. C. (2016). Reverse time migration for microseismic sources using the geometric mean as an imaging condition. *Geophysics*, *81*(2), KS51–KS60. https://doi.org/10.1190/geo2015-0278.1

Payne, S. J., McCaffrey, R., King, R. W., & Kattenhorn, S. A. (2012). A new interpretation of deformation rates in the Snake River Plain and adjacent basin and range regions based on GPS measurements. *Geophysical Journal International*, *189*(1), 101–122. https://doi.org/10.1111/j.1365-246x.2012.05370.x

Pollitz, F. F., Hammond, W. C., & Wicks, C. W. (2020). Rupture Process of the M 6.5 Stanley, Idaho, Earthquake Inferred from Seismic Waveform and Geodetic Data. *Seismological Research Letters*, *92*(2A), 699–709. https://doi.org/10.1785/0220200315

Pollitz, F. F., Wicks, C., Yeck, W. L., & Evans, J. (2019). Fault slip associated with the 2 September 2017 M 5.3 Sulfur Peak, Idaho, earthquake and aftershock sequence. *Bulletin of the Seismological Society of America*, *109*(3), 875–887. https://doi.org/10.1785/0120180206

Rosen, P. A., Hensley, S., Joughin, I. R., Li, F. K., Madsen, S. N., Rodriguez, E., & Goldstein, R. M. (2000). Synthetic aperture radar interferometry. *Proceedings of the IEEE*, *88*(3), 333–382. https://doi.org/10.1109/5.838084

Ross, Z. E., Idini, B., Jia, Z., Stephenson, O. L., Zhong, M., Wang, X., et al. (2019). Hierarchical interlocked orthogonal faulting in the 2019 Ridgecrest earthquake sequence. *Science*, *366*(6463), 346–351. https://doi.org/10.1126/science.aaz0109

Ross, Z. E., Meier, M.-A., & Hauksson, E. (2018). P wave arrival picking and first-motion polarity determination with deep learning. *Journal of Geophysical Research: Solid Earth*, *123*, 5120–5129. https://doi.org/10.1029/2017JB015251

Sethian, J. A., & Popovici, A. M. (1999). 3-D traveltime computation using the fast marching method. *Geophysics*, *64*(2), 516–523. https://doi.org/10.1190/1.1444558

Shen, W., & Ritzwoller, M. H. (2016). Crustal and uppermost mantle structure beneath the United States. *Journal of Geophysical Research: Solid Earth*, *121*, 4306–4342. https://doi.org/10.1002/2016jb012887

Sun, J., Xue, Z., Zhu, T., Fomel, S., & Nakata, N. (2016). Full-waveform inversion of passive seismic data for sources and velocities (pp. 1405–1410). SEG Technical Program Expanded Abstracts.

Thackray, G. D., Rodgers, D. W., & Streutker, D. (2013). Holocene scarp on the Sawtooth fault, central Idaho, USA, documented through lidar topographic analysis. *Geology*, *41*(6), 639–642. https://doi.org/10.1130/g34095.1

Vavryčuk, V. (2015). Moment tensor decompositions revisited. *Journal of Seismology*, *19*(1), 231–252.

Waldhauser, F., & Ellsworth, W. L. (2000). A double-difference earthquake location algorithm: Method and application to the Northern Hayward Fault, California. *Bulletin of the Seismological Society of America*, *90*(6), 1353–1368. https://doi.org/10.1785/0120000006

Wang, R., Diao, F., & Hoechner, A. (2013). SDM-A geodetic inversion code incorporating with layered crust structure and curved fault geometry. EGUGA. EGU2013-2411. https://doi.org/10.3997/2214-4609.20130053

Wei, S., Fielding, E., Leprince, S., Sladen, A., Avouac, J.-P., Helmberger, D., et al. (2011). Superficial simplicity of the 2010 El Mayor-Cucapah earthquake of Baja California in Mexico. *Nature Geoscience*, *4*(9), 615–618. https://doi.org/10.1038/ngeo1213

Wesnousky, S. G. (2006). Predicting the endpoints of earthquake ruptures. *Nature*, *444*(7117), 358–360. https://doi.org/10.1038/nature05275

Withers, M., Aster, R., Young, C., Beiriger, J., Harris, M., Moore, S., & Trujillo, J. (1998). A comparison of select trigger algorithms for automated global seismic phase and event detection. *Bulletin of the Seismological Society of America*, *88*(1), 95–106.

Yang, J., Zhu, H., & Lumley, D. (2020). Time-lapse imaging of coseismic ruptures for the 2019 ridgecrest earthquakes using multiazimuth backprojection with regional seismic data and a 3-d crustal velocity model. *Geophysical Research Letters*, *47*, e2020GL087181. https://doi.org/10.1029/2020GL087181

Ye, L., Lay, T., Kanamori, H., & Rivera, L. (2016). Rupture characteristics of major and great (Mw ≥ 7.0) megathrust earthquakes from 1990 to 2015: 1. Source parameter scaling relationships. *Journal of Geophysical Research Solid Earth*, *121*, 826–844. https://doi.org/10.1002/2015JB012426

Zhang, H., Chen, J., & Ge, Z. (2012). Multi-fault rupture and successive triggering during the 2012 Mw 8.6 Sumatra offshore earthquake. *Geophysical Research Letters*, *39*, L22305. https://doi.org/10.1029/2012GL053805

Supporting Information for "Multi-fault opposing-dip strike-slip and normal-fault rupture during the 2020 M_w 6.5 Stanley, Idaho earthquake"

Jidong Yang[1], Hejun Zhu[2], Thorne Lay[3], Yufeng Niu[4], Lingling Ye[5], Zhong Lu[6],

Bingxu Luo[2], Hiroo Kanamori[7], Jianping Huang[1], Zhenchun Li[1]

[1]Department of Geophysics, China University of Petroleum (East China), Qingdao 266580, China

[2]Department of Geosciences, The University of Texas at Dallas, Richardson, TX 75080, USA

[3]Department of Earth and Planetary Sciences, University of California, Santa Cruz, CA 95064, USA

[4]School of Mining and Geomatics Engineering, Hebei University of Engineering, Handan 056038, China

[5]Department of Earth and Space Sciences, Southern University of Science and Technology, Shenzhen, 518055, China

[6]Roy M. Huffington Department of Earth Sciences, Southern Methodist University, Dallas, TX 75205, USA

[7]Seismological Laboratory, California Institute of Technology, Pasadena, CA 91125, USA

Contents of this file

1. Tables S1 to S2
2. Figures S1 to S8
3. Movies S1 to S3 (additionally attached)

Total Moment Tensor	Component-I	Component-II	Component-III
 USGS NP1=(172°, 74°, -24°) NP2=(269°, 67°, -163°)	 56% DC NP1=(172.2°, 74.0°, -24.8°) NP2=(269.1°, 67.2°, -162.7°)	 44% CLVD NP1=(87.6°, 85.5°, -168.9°) NP2=(356.7°, 79.0°, -4.6°)	
	 60% Major DC NP1=(172.2°,74.0°,-23.8°) NP2=(269.1°,67.2°,-162.7°)	 40% Minor DC NP1=(43.1°,73.0°,-85.2°) NP2=(207.1°,17.6°,-105.3°)	
	 50% Maximum DC NP1=(172.2°,74.0°,-23.8°) NP2=(269.1°,67.2°,-162.7°)	 34% Intermediate DC NP1=(338.6°,47.3°,-50.4°) NP2=(108.0°,55.5°,-124.6°)	 16% Minimum DC NP1=(43.1°,73.1°,94.8°) NP2=(207.1°,17.6°,74.7°)

Table S1: Moment tensor decomposition results for the point-source *W*-phase solution from the USGS-NEIC using different schemes. From top to bottom are double-couple (DC) and compensated linear vector dipole (CLVD), major and minor double-couples, as well as maximum, intermediate and minimum double-couples. The strike, dip, rake of the nodal planes (NP1 and NP2) are listed below the beachballs.

		Hypocenter latitude (°N)	Hypocenter longitude (°W)	Hypocenter depth (km)	Strike(°)	Dip(°)	Subfault along strike, #, size	Subfault along dip, #, size
Single fault		44.465	115.118	10.0	172.3	70.0	15, 4 km	6, 4 km
Two faults	F1	44.333	115.180	13.0	162.9	74.0	8, 4.5 km	7, 3 km
	F2	44.348	115.208	1.23	336.4	60.0	7, 4.5 km	7, 2.9 km

Table S2: Model parameters used in teleseismic finite-fault inversion. Single-fault is for the geometry as shown in Fig. S2, and two-fault is for the geometry as shown in Fig. 3.

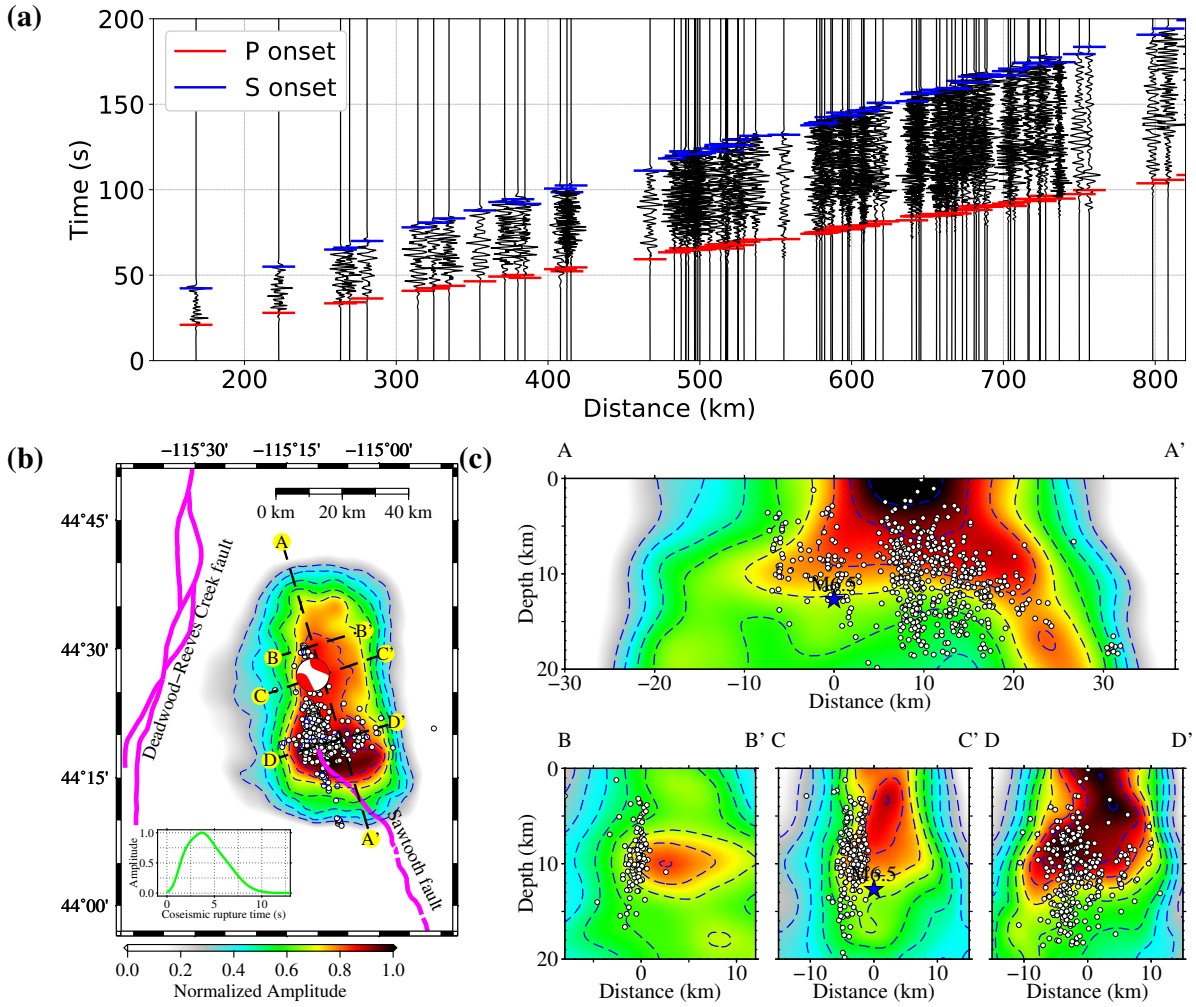

Fig. S1. Normalized cumulative radiated energy calculated with regional multi-azimuth back-projection. (a) Processed regional P-wave records. Blue and red vertical bars denote the P and S-wave onsets, for which the traveltimes are calculated using the fast marching method (Sethian & Popovici, 1999) in a 3D crustal velocity model (Shen & Ritzwoller, 2016). (b) and (c) are normalized cumulative radiated energy in map view and along four vertical profiles, respectively. White dots are the projection of relocated aftershocks in map view and vertical profiles. Note that the distribution of aftershocks is largely anti-correlated with high radiated energy.

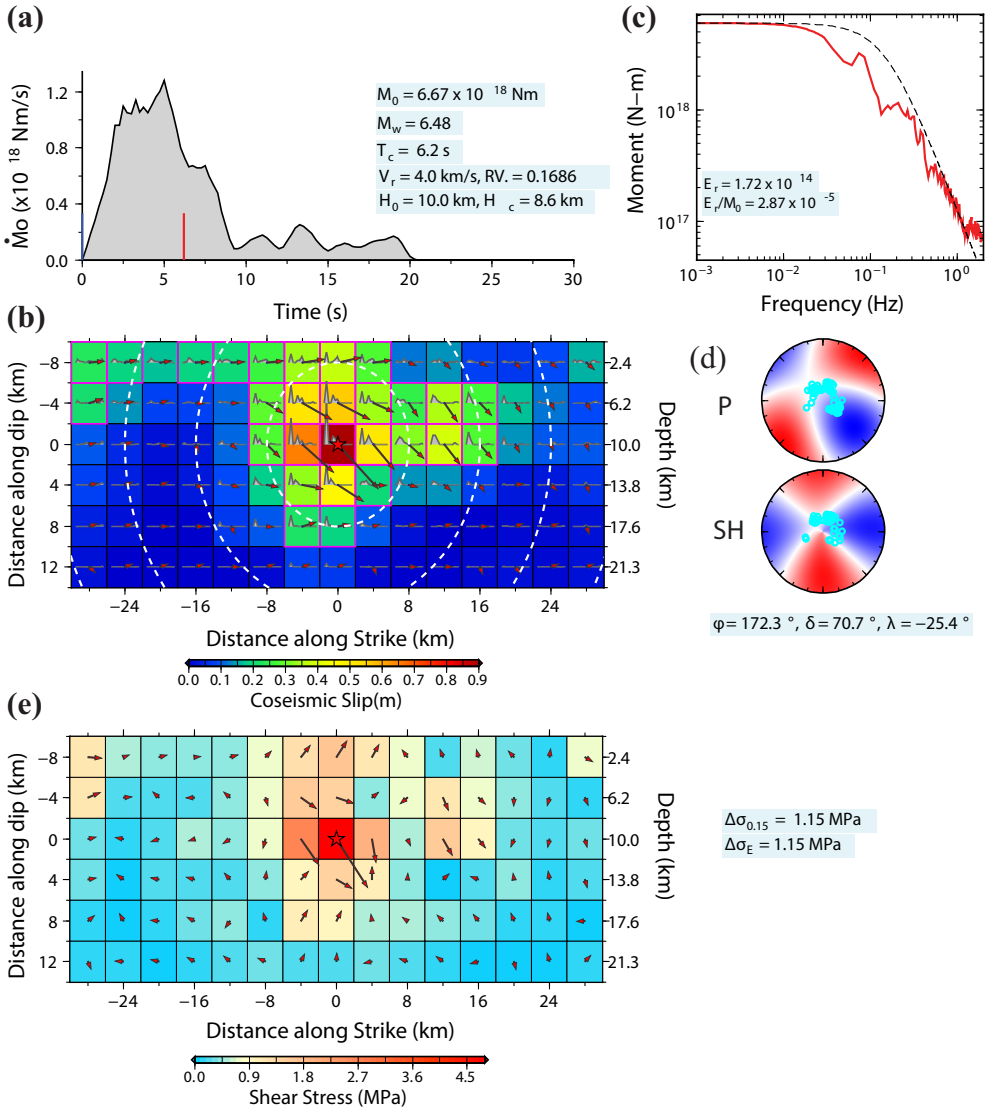

Fig. S2. A single-fault kinematic slip model for the 2020 Stanley earthquake. (a) The moment rate function, along with seismic moment M_w, centroid time T_c (red tick on the time line), imposed kinematic maximum rupture speed V_r, residual variance RV, hypocenter depth H_0 and slip centroid depth H_c. (b) Slip distribution with the average rakes of each subfault patch (vector directions), slip magnitude (vector length and color scale). White dashed lines are 2-s isochrones for the maximum rupture velocity. (c) Source spectrum estimated from the moment rate function spectrum below 0.05 Hz and from stacking of P-wave spectra (after correction for radiation pattern and propagation effects) above 0.05 Hz. E_R denotes radiated energy, and E_R/M_0 denotes moment scaled radiated energy. (d) Lower hemisphere radiation patterns for P and SH waves. Red and blue are compressional and dilational quadrants for P waves, and are clockwise and counter-clockwise quadrants for SH-waves. (e) Shear stress change for the slip model in (b) for a half-space model. $\Delta\sigma_{0.15}$ is the area-truncated circular slip stress drop. $\Delta\sigma_E$ is the slip-weighted stress drop.

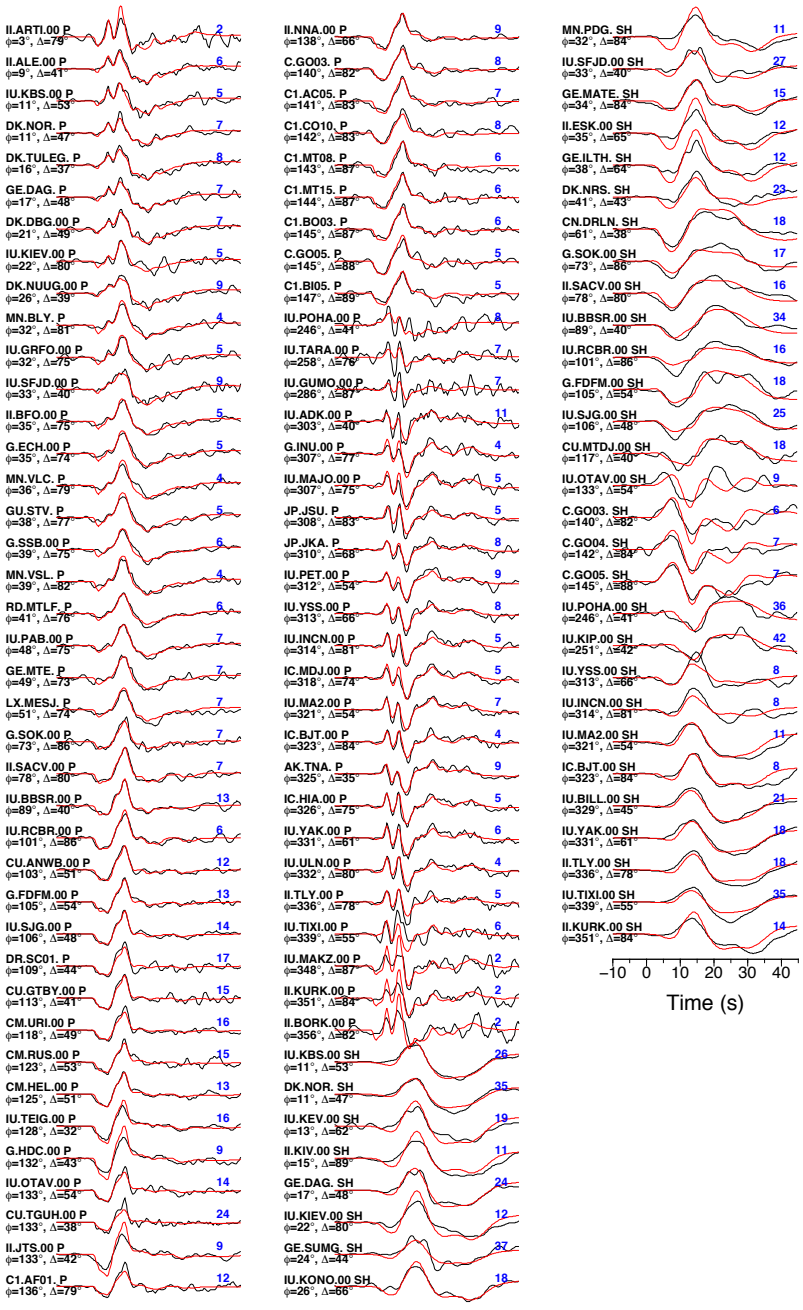

Fig. S3. Comparisons of observed (black) and predicted (red) waveforms for the single-fault slip model shown in Fig. S2. The station names, phase types, along with azimuth and epicenter distances are shown to the left of each comparison. The peak-to-peak amplitude of the data in microns is shown in blue on the right hand side.

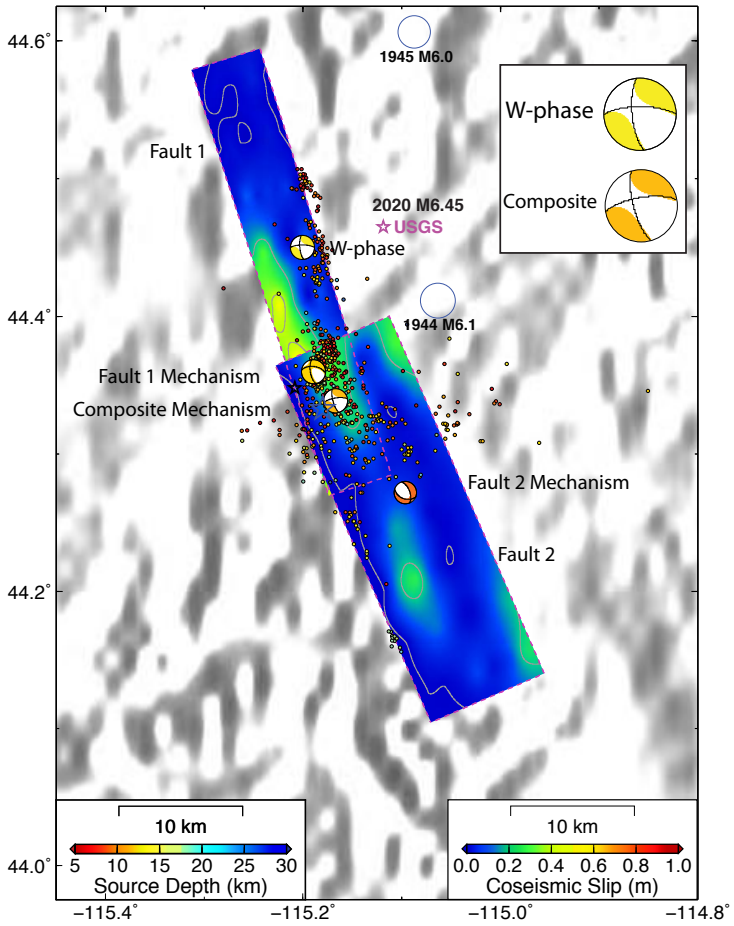

Fig. S4. Map view of the slip model shown in Fig. 3. The magenta star denotes the USGS-NEIC epicenter. The solution from our *W*-phase inversion is shown at its centroid location. The average radiation patterns for the two faults and a composite faulting are shown. Note the similarity of the *W*-phase and composite faulting mechanisms. The relocated aftershocks within one month after the mainshock are superimposed on the slip model. Locations of historic large nearby events are shown by circles with labeled dates.

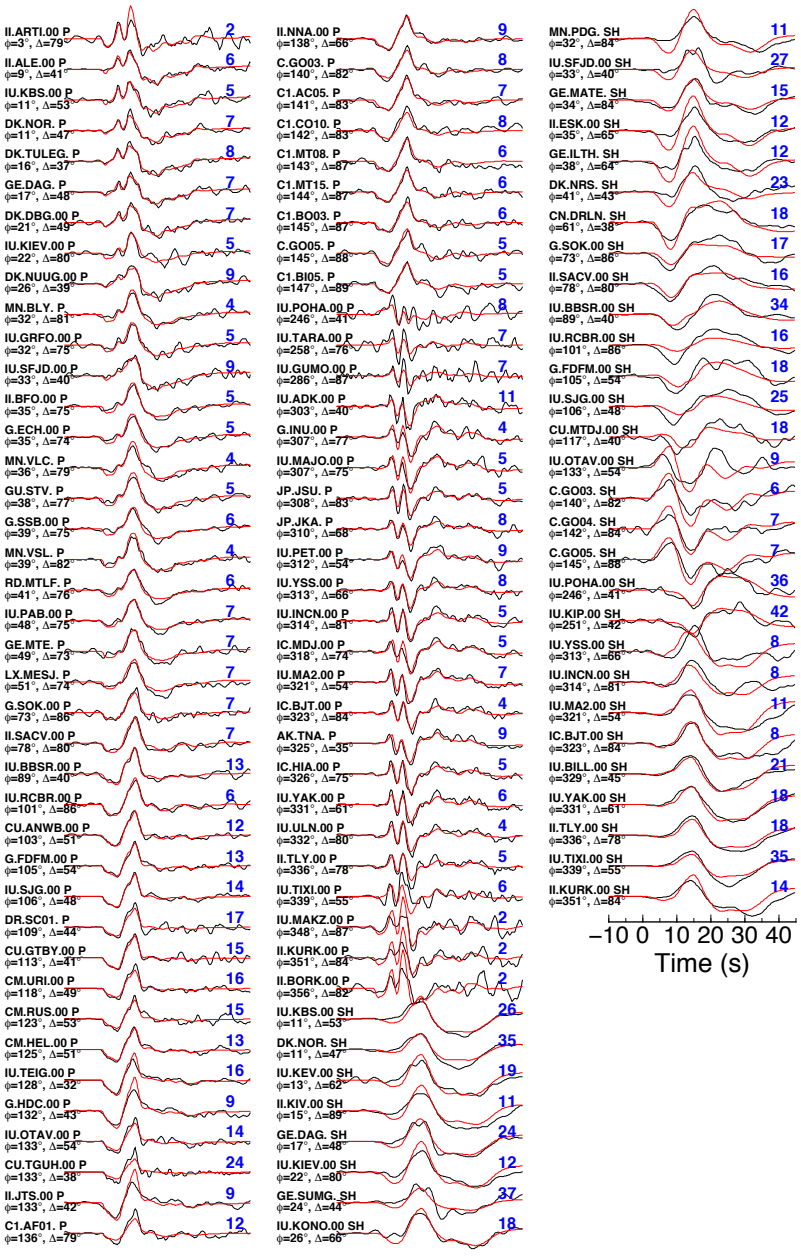

Fig. S5. Comparisons of observed (black) and predicted (red) waveforms for the two-fault slip model shown in Fig. 3. The station names, phase types, along with azimuth and epicenter distances of 72 P and 37 SH phases are shown to the left of each comparison. The peak-to-peak amplitude of the data in microns is shown in blue on the right hand side.

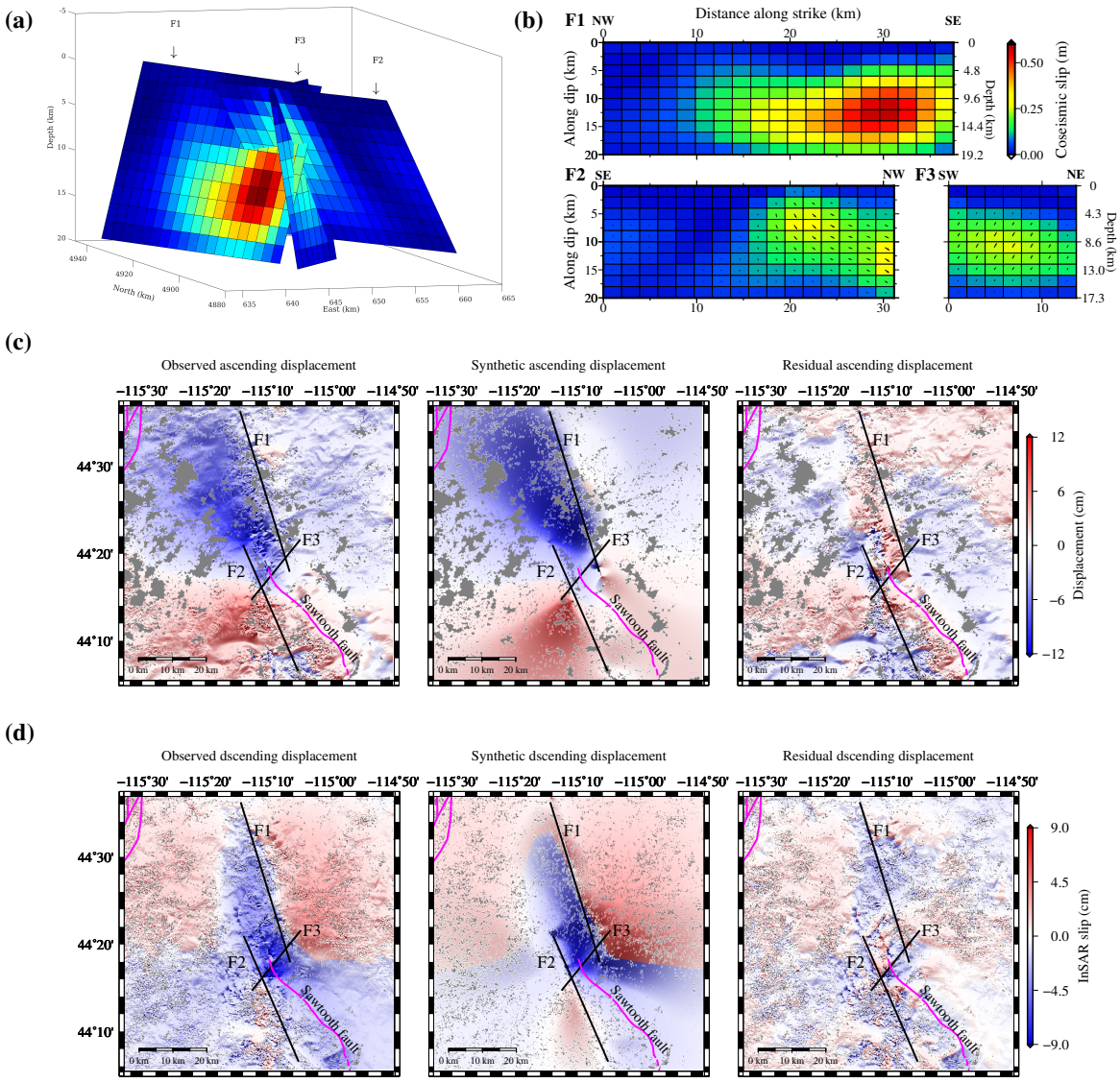

Fig. S6. InSAR analysis results for a three-fault slip model. A third fault about 10 km long is added to the step-over region of the two-fault model shown in Fig. 4. The panel setting is the same as Fig. 4. Note that the third fault has predominantly thrust slip, and the overall maximum slip magnitude is reduced after adding the third fault.

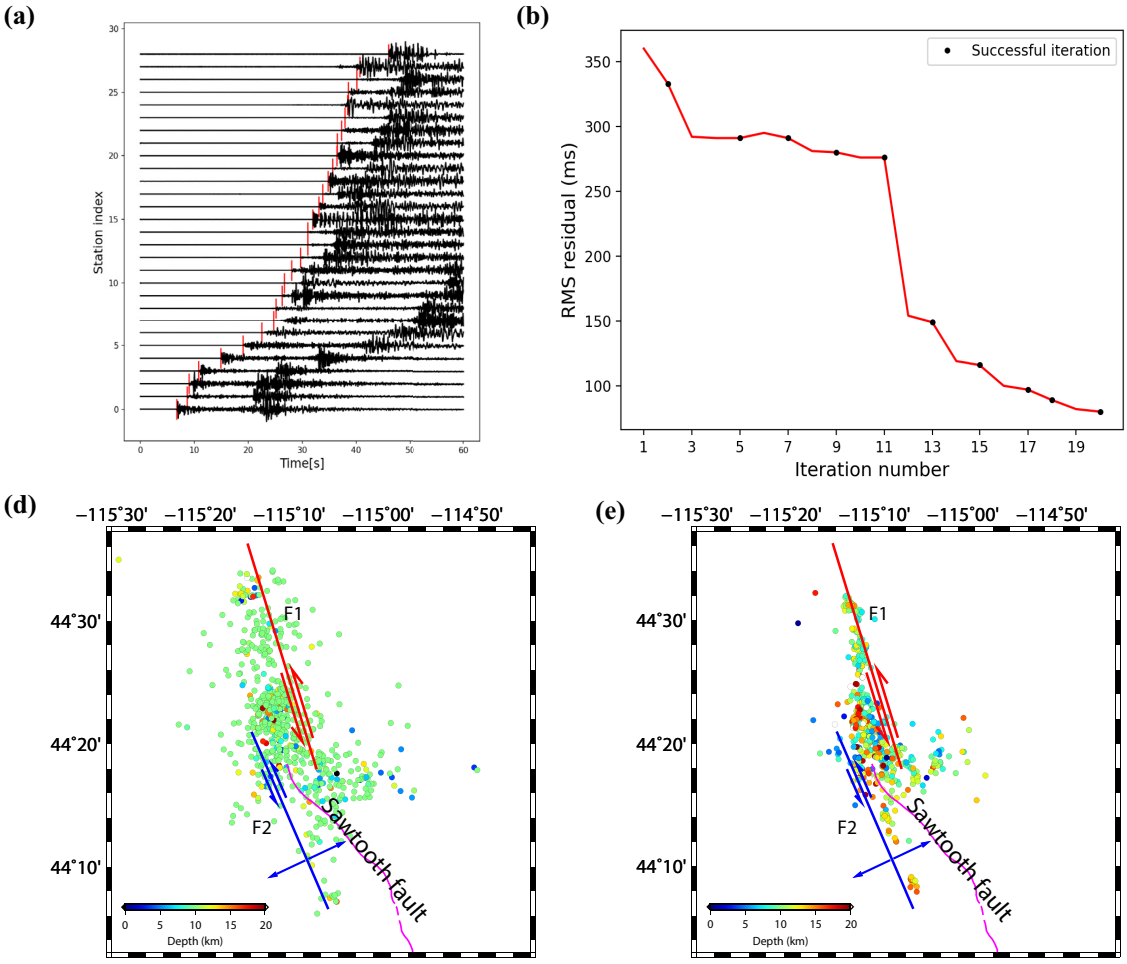

Fig. S7. Relocated aftershocks within one month after the mainshock using a deep-learning-assisted double-difference method. (a) Picked P-wave onsets for a representative event using a deep-learning approach (Ross et al., 2018). (b) Root-mean-square (RMS) residuals of the double-difference travel-time misfit at different iterations. (c) Aftershock location from the USGS-NEIC catalog. (d) double-difference relocated results. Note that significant residual reduction is achieved after the outliers are removed in the first five iterations. The relocated aftershocks in (d) are more focused than those from the USGS-NEIC catalog.

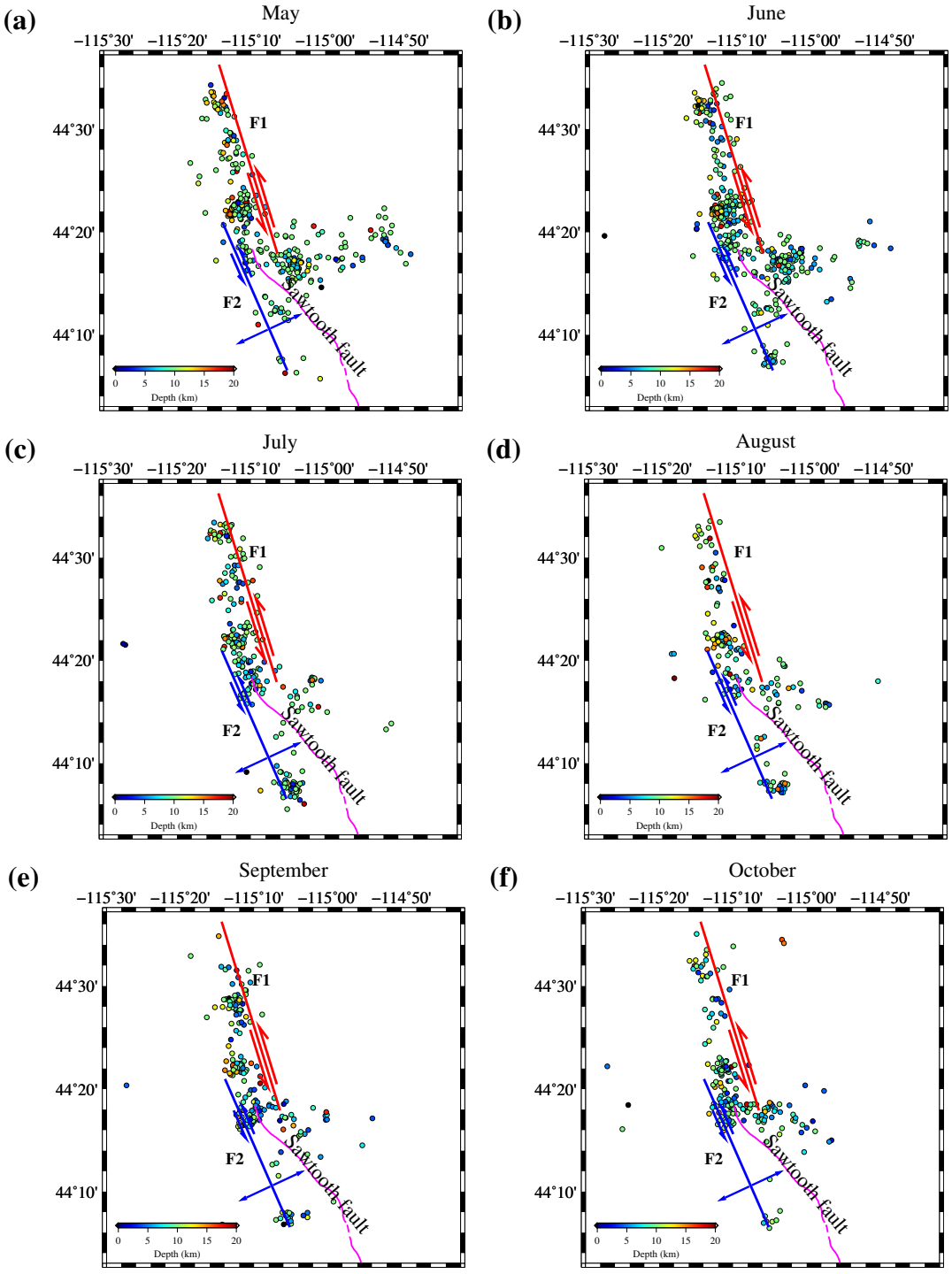

Fig. S8. Evolution of aftershocks from May to October, 2020, downloaded from the USGS-NEIC catalog.

Movie S1. Coseismic rupture propagation imaged from regional multi-azimuth back-projection analysis. The results show that the earthquake first ruptured an unmapped northern subfault F1, then changed to move southwestward (the step-over region), and finally ruptured a southern subfault F2 sub-parallel to the Sawtooth fault scarp.

Movie S2. A 3D slip model computed by finite-fault inversion overlapped with relocated aftershocks (black dots) from different views.

Movie S3. A 3D slip model computed by InSAR analysis overlapped with relocated aftershocks (black dots) from different views.

References

Ross, Z. E., Meier, M.-A., & Hauksson, E. (2018). P Wave Arrival Picking and First-Motion Polarity Determination With Deep Learning. *Journal of Geophysical Research: Solid Earth*, *123*(6), 5120-5129. doi: 10.1029/2017JB015251

Sethian, J. A., & Popovici, A. M. (1999). 3-D traveltime computation using the fast marching method. *Geophysics*, *64*(2), 516-523.

Shen, W., & Ritzwoller, M. H. (2016). Crustal and uppermost mantle structure beneath the United States. *Journal of Geophysical Research: Solid Earth*, *121*(6), 4306–4342.